

# Copper Foil Substrate Enables Planar Indium Plating for Ultrahigh-Efficiency and Long-Lifespan Aqueous Trivalent Metal Batteries

Songyang Chang, Linguo Lu, Irfan Ullah, Wentao Hou, Jose Fernando Florez Gomez, Amanda Conde-Delmoral, Clara M. Font Marin, Gerardo Morell, Zhongfang Chen, and Xianyong Wu\*

Aqueous trivalent metal batteries represent a compelling candidate for energy storage due to the intriguing three-electron transfer reaction and the distinct properties of trivalent cations. However, little research progress has been achieved with trivalent batteries due to the inappropriate redox potentials and drastic ion hydrolysis side reactions. Herein, the appealing yet underrepresented trivalent indium is selected as an advanced metal choice and the crucial effect of substrate on its plating mechanism is revealed. When copper foil is used, an indiophilic indium-copper alloy interface can be formed in situ upon plating, exhibiting favorable binding energies and low diffusion energy barriers for indium atoms. Consequently, a planar, smooth, and dense indium metal layer is uniformly deposited on the copper substrate, leading to outstanding plating efficiency (99.8-99.9%) and an exceedingly long lifespan (6.4–7.4 months). The plated indium anode is further paired with a high-mass-loading Prussian blue cathode (2 mAh cm<sup>-2</sup>), and the full cell (negative/positive electrode capacity, N/P = 2.5) delivers an excellent cycling life of 1000 cycles with 72% retention. This work represents a significant advancement in the development of high-performance trivalent metal batteries.

### 1. Introduction

It is of paramount importance to develop advanced rechargeable battery systems for sustainable and efficient energy

S. Chang, I. Ullah, W. Hou, A. Conde-Delmoral, Z. Chen, X. Wu Department of Chemistry

University of Puerto Rico-Rio Piedras Campus

San Juan, PR 00925-2537, USA E-mail: xianyong.wu@upr.edu

L. Lu, J. F. Florez Gomez, G. Morell Department of Physics

University of Puerto Rico-Rio Piedras Campus

San Juan, PR 00925-2537, USA

C. M. Font Marin

Department of Biochemistry and Genetics

University of Navarra

Pamplona, Navarra 3 1009, Spain

The ORCID identification number(s) for the author(s) of this article can be found under https://doi.org/10.1002/adfm.202407342

DOI: 10.1002/adfm.202407342

storage.[1-3] Lithium-ion batteries have achieved substantial success in electronics and electric vehicles, but the low abundance, high cost, and the flammability restrict their applications.[4,5] Recently, aqueous multivalent metal batteries (AMMBs) have attracted increasing attention as competitive candidates for energy storage, because the high capacity and low potential of metal electrodes endow them with high energy density.[6-8] Moreover, aqueous electrolytes are nonflammable, cost-effective, and environmentally friendly, and they exhibit 1-2 orders of magnitude higher ionic conductivity than non-aqueous ones.[9,10] These properties further motivate researchers to seek high-performance metal electrodes for aqueous multivalent batteries.

The selection of the metal element plays a vital role in determining battery performance. Currently, research efforts are concentrated on divalent transition metal systems. Zinc (Zn),

in particular, has garnered extensive interest due to its high capacity (820 mAh  $g^{-1}$ ), low potential (-0.76 V vs standard hydrogen electrode, SHE), and non-toxicity.[11,12] However, Zn is susceptible to dendrite growth, parasitic hydrogen evolution reaction (HER), and metal corrosion, which significantly hinder its practical application. [13,14] Consequently, researchers are redirecting their attention to alternative transition metals such as iron (Fe), nickel (Ni), manganese (Mn), and copper (Cu), hoping to find an eligible anode for AMMBs. To date, many interesting results have been achieved, but there are some intrinsic drawbacks that are challenging to address. For instance, Fe<sup>2+</sup> ions are good reducing agents, which can be easily oxidized by dissolved oxygen or high-voltage cathodes. Hence, low cell voltages are commonly observed in Fe metal batteries (0.4-0.8 V).[15-18] Akin to Zn, nickel is prone to electrode passivation, and its notable plating overpotential (400 mV) decreases the round-trip energy efficiency.[19-21] Although Mn is cheap and non-toxic, its low potential (-1.18 V vs SHE) inevitably incurs HER and low efficiency at practical current densities (1–2 mA cm<sup>-2</sup>). [22–24] The Cu<sup>2+</sup> insertion chemistry is intriguing, which imparts 4-electron reactions and ultrahigh

16163028, 0, Downloaded from https://onlinelibrary.wiley.com/doi/10.1002/adfm.202407342 by jim jim - University Of British Columbia , Wiley Online Library on [02.07/2024]. See the Terms and Conditions (https://onlinelibrary.wiley.com/rerms

and-conditions) on Wiley Online Library for rules of use; OA articles are governed by the applicable Creative Commons License

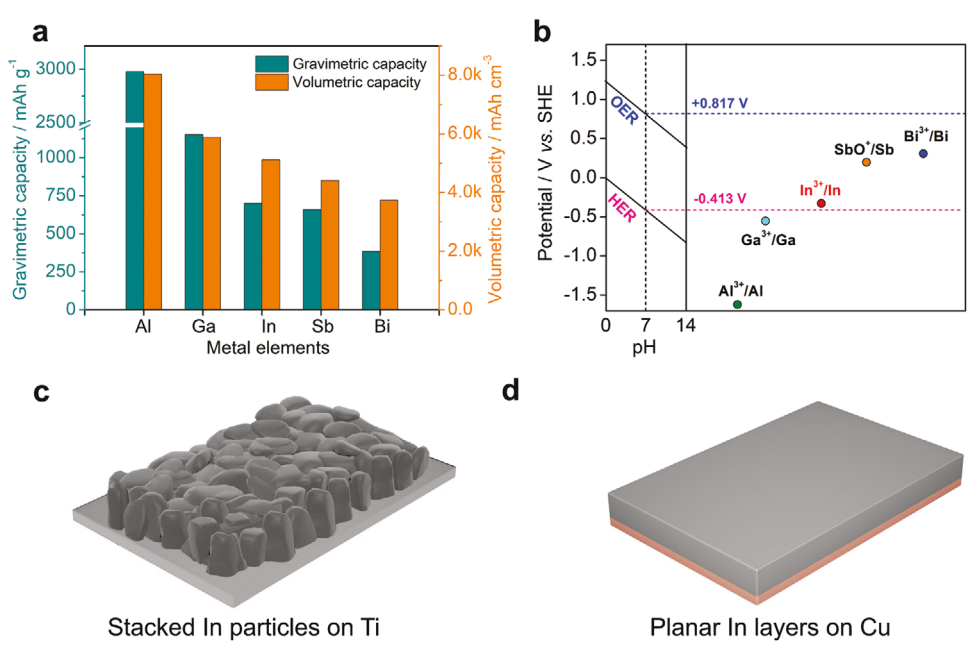


Figure 1. a) The gravimetric and volumetric capacities of trivalent metals. (b) The E-pH diagram of water and M<sup>3+</sup>/M redox potentials. c) The particlestacking morphology of indium on the titanium foil. d) The planar foil-like morphology of indium on the copper foil.

capacities in sulfide/selenide-based cathode materials;[25-27] however, the high Cu<sup>2+</sup>/Cu potential (+0.34 V vs SHE) precludes it as an attractive anode.[28,29]

In contrast, aqueous trivalent metal batteries represent a promising but underexplored direction within the aqueous battery landscape. Their three-electron transfer reaction holds the potential to boost the electrode capacity, thereby improving battery energy density. Furthermore, trivalent cations exhibit distinct physicochemical properties, [6,30,31] such as ionic radius, charge density, and chemical bonding, which may lead to the discovery of novel redox chemistries and plating mechanisms. In the trivalent metal context, aluminum (Al) is an appealing contender due to its predominantly high capacity of 2980 mAh g<sup>-1</sup> (Figure 1a).[32] However, the ultralow potential of Al3+/Al couple (-1.66 V vs SHE) lies far outside the water stability window (Figure 1b), resulting in considerable HER side reactions.[33] The aluminum-water incompatibility accounts for sporadic reports and insufficient success of aqueous Al metal batteries. Aside from Al, only a few trivalent metals are available, including antimony (Sb), bismuth (Bi), gallium (Ga), and indium (In), all showing good capacities of 384-1153 mAh g<sup>-1</sup> (Figure 1a and Table S1, Supporting Information). Nevertheless, Sb3+ and Bi<sup>3+</sup> ions are vulnerable to hydrolysis, [34,35] yielding precipitation compounds instead of transparent solutions. Additionally, their relatively high potentials (0.2-0.308 V vs SHE, Figure 1b) compromise the full cell voltage. Gallium shows promise from the capacity and potential perspective, but its low melting point (29.8 °C) poses significant challenges in practical temperature conditions.[36] In comparison, indium (In) metal stands out as an attractive choice, which not only possesses a high capacity (≈700 mAh  $g^{-1}$ ) but also a suitable redox potential (-0.34 V vs SHE) that is within the water electrochemical window. Moreover, various indium salts, including chlorides, bromides, and iodides, are highly soluble in water without hydrolysis issues (Table S2, Supporting Information). Based on these considerations, it is indispensable to investigate the In plating mechanism to propel the development of aqueous trivalent metal batteries.

In this work, we examined the effect of substrates on the In plating mechanism in the 1.0 M InCl<sub>3</sub> electrolyte. Titanium foil enabled a satisfactory particle-stacking morphology (Figure 1c) with a high efficiency of 99.3-99.5%, whereas copper foil produced an optimal planar foil-like morphology (Figure 1d) with a superb efficiency of 99.8-99.9%. Furthermore, the asymmetrical indium-copper battery achieves an ultralong lifespan of 6.4-7.4 months without short-circuits or battery failure, indicating an extremely reversible plating process. Physical characterizations and DFT calculations reveal that an indiophilic InCu alloy interface is in situ generated during plating, which exerts a favorable binding affinity toward indium atoms and subsequently promotes their in-plane growth. When the plated indium was coupled with high-mass-loading Prussian blue cathode (2.0 mAh cm<sup>-2</sup>), the full cell (N/P = 2.5) delivered an outstanding cycling life of 1000 cycles with 72% retention. Our work represents a significant step toward the development of high-performance aqueous trivalent metal batteries.

## 2. Results and Discussion

The choice of substrate is of critical importance for metal plating. In this work, we first utilized titanium (Ti) foil for In plating, due to its high material stability and chemical inertness. The 1.0 м indium chloride (InCl<sub>3</sub>) electrolyte is a transparent solution without hydrolysis side reactions (Figure S1, Supporting Information). This electrolyte is mildly acidic (pH  $\approx$  2.0) with a reasonable ionic conductivity of ≈16 mS cm<sup>-1</sup> (Figure S2, Supporting Information). To gain more insights into the In plating behavior, we examined its plating efficiency at various capacities (1, 5, and 10 mAh cm<sup>-2</sup>) with a current of 1.0 mA cm<sup>-2</sup>. Figure 2a

16163028,0, Downloaded from https://onlinelibrary.wiley.com/doi/10.1002/adfm.202407342 by jim jim - University Of British Columbia , Wiley Online Library on [02/07/2024]. See the Terms

ns) on Wiley Online Library for rules of use; OA articles are governed by the applicable Creative Common

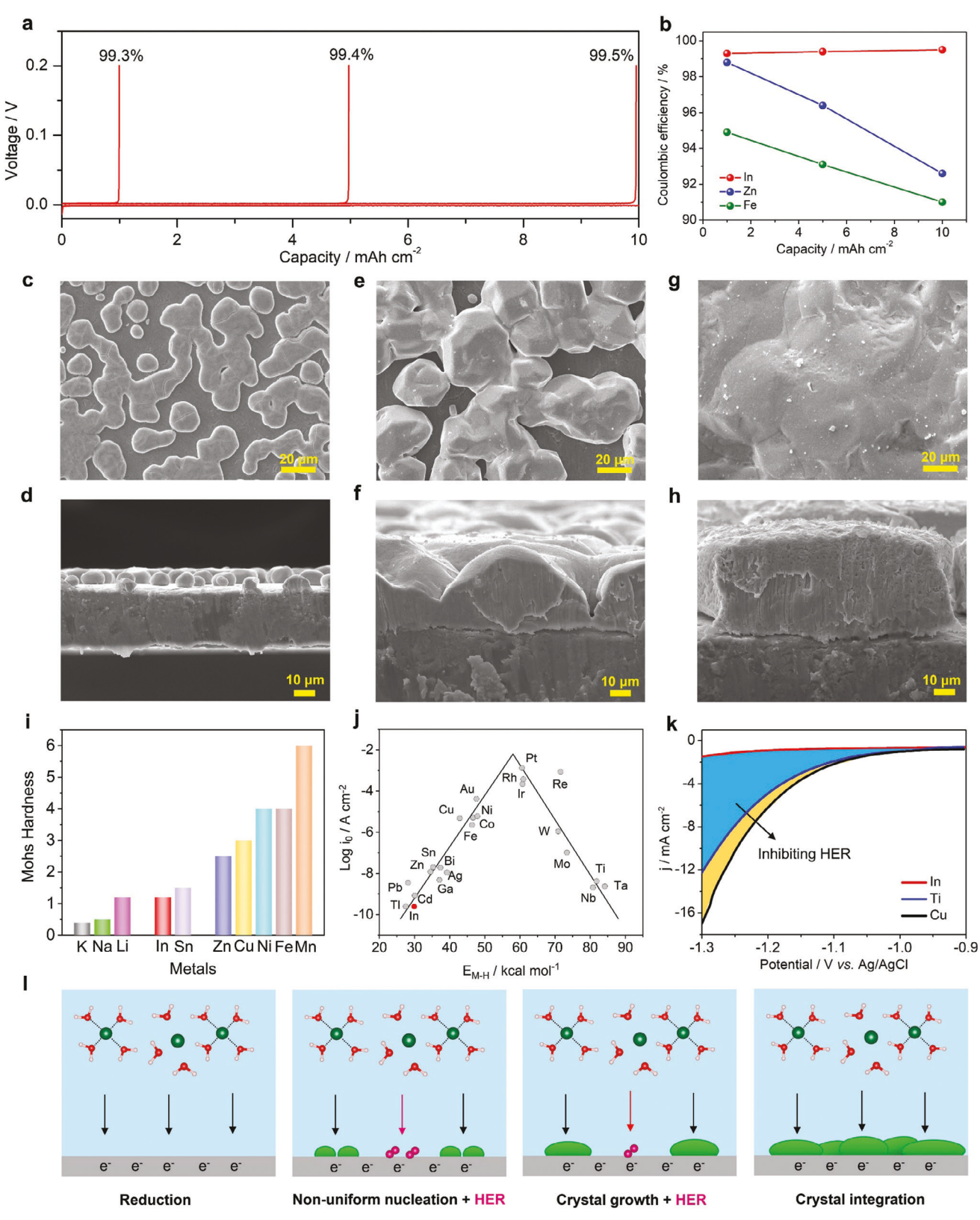


Figure 2. The In plating behavior on the Ti foil. a) Typical GCD curves of In||Ti batteries at 1 mA cm<sup>-2</sup> with different capacities. b) The capacity-efficiency correlation of different metals. c,d) SEM images of In at 1 mAh cm<sup>-2</sup>. e,f) SEM images of In at 5 mAh cm<sup>-2</sup>. g,h) SEM images of In at 10 mAh cm<sup>-2</sup>; i) Mohs hardness of metals. j) Volcano plot for the hydrogen evolution reaction, reproduced with permission. Copyright 1972, Elsevier. k) LSV curves of In, Ti, and Cu in an HCI/NaCl mixture solution. l) The scheme of the In plating process on the Ti foil.

www.afm-journal.de

1616928, D. Downloaded from https://onlinelibrary.wiley.com/doi/10.1002/adfm.202407342 by jim jim - University Of British Columbia, Wiley Online Library on [02.07/2024]. See the Terms and Conditions (https://onlinelibrary.wiley.com/crams-and-conditions) on Wiley Online Library for rules of use; OA articles are governed by the applicable Creative Commons Licasson (https://onlinelibrary.wiley.com/crams-and-conditions) on Wiley Online Library for rules of use; OA articles are governed by the applicable Creative Commons Licasson (https://onlinelibrary.wiley.com/crams-and-conditions) on Wiley Online Library for rules of use; OA articles are governed by the applicable Creative Commons Licasson (https://onlinelibrary.wiley.com/crams-and-conditions) on Wiley Online Library for rules of use; OA articles are governed by the applicable Creative Commons Licasson (https://onlinelibrary.wiley.com/crams-and-conditions) on Wiley Online Library for rules of use; OA articles are governed by the applicable Creative Commons Licasson (https://onlinelibrary.wiley.com/crams-and-conditions) on Wiley Online Library for rules of use; OA articles are governed by the applicable Creative Commons Licasson (https://onlinelibrary.wiley.com/crams-and-conditions) on Wiley Online Library for rules of use; OA articles are governed by the applicable Creative Commons Licasson (https://onlinelibrary.wiley.com/crams-and-conditions) on Wiley Online Library for the applicable Creative Commons Licasson (https://onlinelibrary.wiley.com/crams-and-conditions) on Wiley Online Library for the applicable Creative Commons Licasson (https://onlinelibrary.wiley.com/crams-and-conditions) on Wiley Online Library for the applicable Creative Commons Licasson (https://onlinelibrary.wiley.com/crams-and-conditions) on Wiley Online Library for the applicable Creative Commons Licasson (https://onlinelibrary.wiley.com/crams-and-conditions) on Wiley Online Library for the applicable Creative Commons Licasson (https://onlinelibrary.wiley.com/crams-and-conditions) on Wiley O

and Figure S3 (Supporting Information) display galvanostatic charge/discharge (GCD) curves of these In||Ti batteries. Interestingly, the increment of capacity results in a higher plating efficiency, where the average efficiency is 99.3%, 99.4%, and 99.5% at 1, 5, and 10 mAh cm<sup>-2</sup>, respectively. This capacity-efficiency correlation is quite counterintuitive (Figure 2b), as a higher plating capacity usually leads to inferior efficiency for most metal electrodes.<sup>[37–39]</sup> For instance, the asymmetrical Zn||Ti battery exhibits efficiencies of 98.8%, 96.4%, 92.6% at 1, 5, and 10 mAh cm<sup>-2</sup>, respectively (Figure S4, Supporting Information). The Fe metal also encounters a similar efficiency decrease issue (Figure S5, Supporting Information). This peculiar property motivates us to investigate the In plating morphology, which notably impacts the plating efficiency.

Scanning electron microscopy (SEM) images at these conditions are given in Figure 2c–h. As shown, at 1 mAh cm<sup>-2</sup>, the deposited In metal particles have a sphere-like morphology, which are moderately connected with each other. The average size for each particle is 10– $20\,\mu m$ . The spherical morphology and particle size is further corroborated by cross-sectional SEM (Figure 2d). At this stage, In particles cannot fully cover the Ti foil, and the substrate surface is relatively empty. At 5 mAh cm<sup>-2</sup> capacity, In metals further grow into densely packed and well-connected chunks (Figure 2e,f), and their particle size increases to  $\approx 50\,\mu m$ . Meanwhile, the Ti foil surface is almost fully covered. At  $10\,mAh$  cm<sup>-2</sup> capacity (Figure 2e), all previous indium chunks "melt" or "weld" with each other and eventually evolve into an intact foil-like deposition layer. Its surface is quite smooth, and the stacking manner is dense (Figure 2g,h).

It is interesting to observe the morphological transition from stacked particles to a planar foil, which should be related to the intrinsic mechanical properties of In. Unlike conventional transition metals (Fe, Cu, and Zn) that are stiff and rigid, In is a soft, elastic, and ductile post-transition metal, which has a Mohs hardness of 1.2 (Figure 2i). [40] This value is comparable to that of alkali metals (Li, Na, and K) but much smaller than transition metals (2.5–8.5). Under the coin cell testing conditions, the moderate stack pressure may promote micro-sized In chunks to integrate with each other, eventually forming a planar metal layer. Indeed, we find that after grinding In powders in a mortar for 15 min, these microsized particles become visually sticky (Figure S6, Supporting Information), and they convert from the particle stacking to planar foil morphology (Figure \$7, Supporting Information). In contrast, Zn powders cannot transform into a planar foil, which still appear as dispersed particles with smaller size (Figures S8 and S9, Supporting Information). The mechanical softness contributes to the unique morphological evolution of In

The morphological transition also explains the enhanced efficiency of In at higher capacities. First, compared with stacked particles, a planar foil can dramatically reduce its surface area and decrease contact with electrolytes, [41,42] thus benefiting the plating efficiency. Second, the anti-HER property of In further contributes to its improved efficiency. In the catalysis field, there exists a prominent volcano plot (Figure 2j), [43-45] where the optimal HER catalyst is platinum, and poor catalysts include lead, indium, and cadmium. To verify this hypothesis, we conducted linear scanning voltammetry (LSV, Figure 2k and Figure S10, Supporting Information) using three metal foils (In, Ti, and Cu)

in a slightly acidic chloride electrolyte, whose pH value (2.0) is identical to 1.0 m InCl $_3$ . At a negative potential of -1.30 V versus Ag/AgCl, In metal causes a low cathodic current of 1.5 mA cm $^{-2}$ , markedly smaller than Cu (17.0 mA cm $^{-2}$ ) and Ti (12.2 mA cm $^{-2}$ ), which indicates the suppressed HER side reaction. Therefore, when Ti foil is covered by more In metals at higher capacities, the strong HER resistance reinforces the In efficiency accordingly. In contrast, Zn metal lacks an efficient anti-HER capability, and its overall plating morphology is much inferior (Figure S11, Supporting Information), leading to lower efficiencies at higher capacities.

Based on these results, the In plating on Ti is illustrated in Figure 2l. From 1 to 10 mAh cm $^{-2}$ , the mechanically soft and HER-resistant In metal progressively converts from stacked particles to a planar foil, thus boosting the efficiency from 99.3% to 99.5%. Unfortunately, the Ti foil cannot sustain long-term cycling at 10 mAh cm $^{-2}$ , and In||Ti batteries experience short-circuits after 48 cycles (960 h, Figure S12, Supporting Information). We reason that the relatively protruding edges of In particles could penetrate the separator, thus causing a soft short circuit. Figure S13 (Supporting Information) provides SEM images of the glass fiber separator, whose pore size ranges from 5 to 15  $\mu$ m, which is comparable to the sharp edge of In particles. Therefore, it is imperative to remedy this issue to realize high efficiency and high capacity simultaneously, both of which are desirable for practical applications.

The above results also suggest that In metal exhibits a high tendency to nucleate and grow on initial In metal sites, which then further emerge or integrate into a foil-like texture. Thus, we hypothesize that if the initial nucleation process is facilitated, there will be plenty of In "seeds" for the following crystal growth, leading to an optimal planar foil morphology at various capacities (Figure 3a). Moreover, the full coverage of anti-HER In metal on the substrate surface can minimize side reactions, further enhancing the plating efficiency. Previous studies have reported that certain substrates can form favorable alloy interfaces with plating metals, thereby reducing the nucleation energy barrier and facilitating the nucleation process. [46-48] Herein, we switched to the Cu foil, aiming to leverage the In–Cu alloy formation [49,50] for optimal planar plating.

As anticipated, the Cu foil significantly alters the plating morphology, resulting in a planar foil morphology at all testing capacities. At 1 mAh cm<sup>-2</sup>, the entire Cu foil is completely covered with In metal, and the In surface is notably flat (Figure 3b). There are some gaps between these metal layers, possibly due to the moderate plating capacity. Cross-sectional SEM further confirms the flat, uniform, and dense In deposition layer (Figure 3c), with an approximate thickness of 11 µm. The original Cu foil is 9 µm thick, indicating that the plated In metal is approximately 2 µm thick. Based on the specific capacity ( $\approx$ 700 mAh g<sup>-1</sup>) and density (7.29 g cm<sup>-3</sup>) of In, we can calculate that a 2 µm thickness corresponds to 1.03 mAh cm<sup>-2</sup>, which aligns well with the practical capacity. This suggests that the plated In metal is densely packed on the Cu foil. Figure \$14 (Supporting Information) shows the cross-sectional EDS mapping analysis of the In@Cu electrode, which clearly illustrates the distribution of In metal layers on the Cu foil substrate. Furthermore, it is noteworthy that the planar morphology is markedly different from the spherical particles observed on the Ti foil (Figure 2c,d), which

16163028, 0, Downloaded from https://onlinelibrary.wiley.com/doi/10.1002/adfm.202407342 by jim jim - University Of British Columbia, Wiley Online Library on [02.07/2024]. See the Terms and Condit

) on Wiley Online Library for rules of use; OA articles are governed by the applicable Creative Commons License

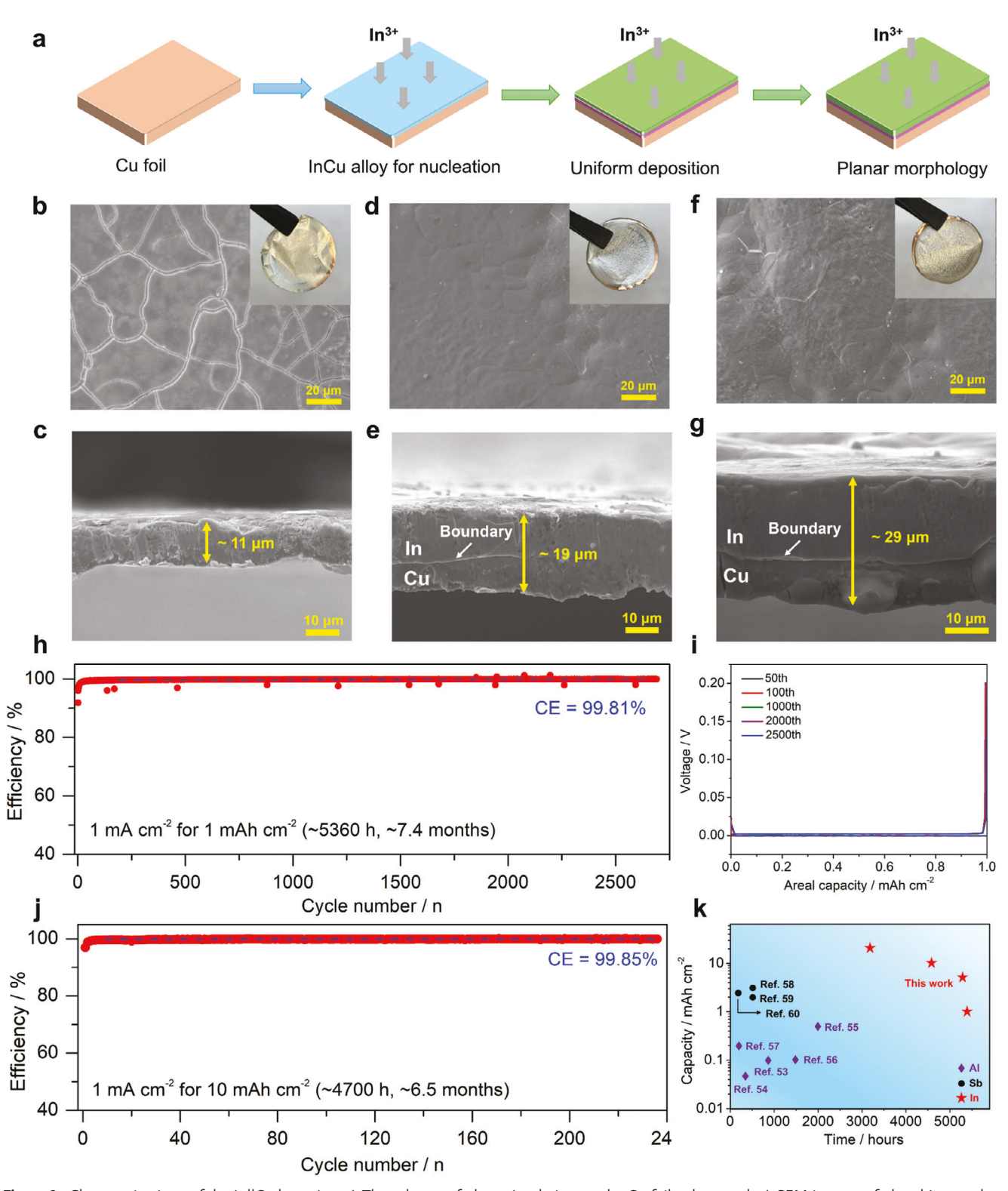


Figure 3. Characterizations of the In||Cu batteries. a) The scheme of planar In plating on the Cu foil substrate. b,c) SEM images of plated In metal at 1 mAh cm<sup>-2</sup>. d,e) SEM images of plated In metal at 5 mAh cm<sup>-2</sup>. f,g) SEM images of plated In metal at 10 mAh cm<sup>-2</sup>. h) The cycling performance of In||Cu batteries at 1 mAh cm<sup>-2</sup>. i) Selected GCD curves during cycling at 1 mAh cm<sup>-2</sup>. j) The cycling performance of In||Cu batteries at 10 mAh cm<sup>-2</sup>. k) The time-capacity performance comparison between different trivalent metal electrodes.

www.afm-journal.de

1616928, D. Downloaded from https://onlinelibrary.wiley.com/doi/10.1002/adfm.202407342 by jim jim - University Of British Columbia, Wiley Online Library on [02.07/2024]. See the Terms and Conditions (https://onlinelibrary.wiley.com/crams-and-conditions) on Wiley Online Library for rules of use; OA articles are governed by the applicable Creative Commons Licasson (https://onlinelibrary.wiley.com/crams-and-conditions) on Wiley Online Library for rules of use; OA articles are governed by the applicable Creative Commons Licasson (https://onlinelibrary.wiley.com/crams-and-conditions) on Wiley Online Library for rules of use; OA articles are governed by the applicable Creative Commons Licasson (https://onlinelibrary.wiley.com/crams-and-conditions) on Wiley Online Library for rules of use; OA articles are governed by the applicable Creative Commons Licasson (https://onlinelibrary.wiley.com/crams-and-conditions) on Wiley Online Library for rules of use; OA articles are governed by the applicable Creative Commons Licasson (https://onlinelibrary.wiley.com/crams-and-conditions) on Wiley Online Library for rules of use; OA articles are governed by the applicable Creative Commons Licasson (https://onlinelibrary.wiley.com/crams-and-conditions) on Wiley Online Library for rules of use; OA articles are governed by the applicable Creative Commons Licasson (https://onlinelibrary.wiley.com/crams-and-conditions) on Wiley Online Library for the applicable Creative Commons Licasson (https://onlinelibrary.wiley.com/crams-and-conditions) on Wiley Online Library for the applicable Creative Commons Licasson (https://onlinelibrary.wiley.com/crams-and-conditions) on Wiley Online Library for the applicable Creative Commons Licasson (https://onlinelibrary.wiley.com/crams-and-conditions) on Wiley Online Library for the applicable Creative Commons Licasson (https://onlinelibrary.wiley.com/crams-and-conditions) on Wiley Online Library for the applicable Creative Commons Licasson (https://onlinelibrary.wiley.com/crams-and-conditions) on Wiley O

highlights the crucial role of the substrate in the In plating process.

At 5 mAh cm<sup>-2</sup> (Figure 3d), the previous metal gaps vanish. and the In metal appears as an integral, smooth, and crackfree foil, surpassing the morphology observed on Ti foil. Crosssectional SEM reveals that the plated In is densely packed without appreciable voids or gaps (Figure 3e), and the entire In@Cu thickness is approximately 19 µm. Thus, the plated In has a thickness of  $\approx 10 \, \mu \text{m}$ , corresponding to a capacity of  $\approx 5.1 \, \text{mAh cm}^{-2}$ , which closely aligns with the practical capacity. Even at a high capacity of 10 mAh cm<sup>-2</sup> (Figure 3f,g), the In metal maintains a uniform, planar, and dendrite-free foil morphology. The In@Cu thickness measures ≈29 µm, suggesting that the In metal is approximately 20 µm thick. This is consistent with the theoretical thickness of 19.6 µm at 10 mAh cm<sup>-2</sup>. Digital photos are provided in the figure inset, displaying shinny metallic surfaces. We also examined more SEM images of In metal at various plating capacities, specifically 0.2, 0.5, 2, and 3 mAh cm<sup>-2</sup>, to gain a more comprehensive and detailed understanding of the In plating process. As shown in Figure \$15 (Supporting Information), the Cu foil consistently demonstrated a planar and dense morphology across all tested capacities. In contrast, the Ti foil exhibited an obvious particle-stacking morphology. Future efforts will focus on in situ experiments to better observe the In plating process and dynamics.

The optimal planar morphology not only minimizes the surface area but also avoids the short circuit issue, leading to exceptional plating efficiency and cycling stability. As shown in Figure 3h, the average efficiency reaches an impressive value of 99.81% over 2680 cycles (calendar life: 5360 h, 7.4 months) at 1 mAh cm<sup>-2</sup> capacity, surpassing the 99.3% efficiency observed on Ti foil. Importantly, there are few data points exceeding 100% in the Cu foil case, a phenomenon commonly observed in In||Ti batteries (Figure \$16, Supporting Information), indicating the circumvention of soft short circuits. Figure 3i presents selected GCD curves at the 50<sup>th</sup>, 100<sup>th</sup>, 1000<sup>th</sup>, 2000<sup>th</sup>, and 2500<sup>th</sup>, which are well overlapped without noticeable polarization increment, further confirming the plating stability.

The average efficiency is 99.82% at 5 mAh cm<sup>-2</sup> over 527 cycles (calendar life: 5270 h, 7.3 months, Figure \$17, Supporting Information), which further increases to 99.85% at 10 mAh cm<sup>-2</sup> (calendar life: 4600 h, 6.4 months), as demonstrated in Figure 3 and Figure \$18 (Supporting Information). Even at an ultrahigh plating capacity of 20 mAh cm<sup>-2</sup>, the In||Cu battery maintains a high efficiency of 99.72% over 79 cycles (calendar life: 3160 h, 4.4 months, Figure \$19, Supporting Information), which proves the efficacy of planar plating in stabilizing the metal plating process. In contrast, the In||Ti battery easily gets short-circuited at 20 mAh cm<sup>-2</sup> (Figure \$20, Supporting Information). Besides the high capacity, the Cu foil supports high efficiency at higher current densities. As shown in Figure S21 (Supporting Information), the efficiency further improves to 99.9% at 2 mA cm<sup>-2</sup>, likely due to the kinetic suppression of HER side reactions. At 4 mA cm<sup>-2</sup>, the efficiency remains high at 99.9% (Figure S22, Supporting Information), suggesting its potential for high-power applications.

We underline that these In||Cu batteries achieve an impressive calendar life, which is another crucial parameter for determining the reaction reversibility in aqueous batteries. [51,52] Some publications have used high currents to mask HER side reactions, resulting in long cycling numbers but short calendar life. For instance, with a high current (10 mA cm<sup>-2</sup>) and moderate capacity (1 mAh cm<sup>-2</sup>) is used, it takes only 200 h to complete 1000 cycles. In our study, In||Cu cells at 1, 5, and 10 mAh cm<sup>-2</sup> have been cycled for 4600-5360 h, corresponding to 6.4-7.4 months.

The high capacity, high efficiency, and long calendar life collectively position In as an outstanding choice in the context of aqueous trivalent metal batteries, as compared in Figure 3k and Table S3 (Supporting Information). Although Al possesses a very high capacity, the low potential drastically limits its application. Consequently, most aqueous Al batteries are tested in symmetrical Al (or Al-alloy) battery configurations, [53-57] and critical Coulombic efficiency information is unavailable. Despite this, their plating capacity and calendar life are typically limited to 0.2 mAh cm<sup>-2</sup> and 1500 h. Recently, Sb metal has emerged as a candidate for aqueous trivalent batteries, [58-60] offering a higher capacity of 1-2 mAh cm<sup>-2</sup> and reasonable efficiency of 91-99.4%. However, it encounters a short calendar life of 200-500 h, possibly due to the corrosion of alkaline electrolytes. In contrast, In metal exhibits remarkable capacity (1-10 mAh cm<sup>-2</sup>), efficiency (>99.8%), and calendar life (6.4-7.4 months) through the straightforward use of InCl3 electrolyte and Cu foil, highlighting its advantages over these trivalent candidates.

Except the Cu foil, we discover that other metal substrates may achieve similar planar plating behavior. For instance, when a tin (Sn) foil is used, the In metal also shows a flat, dense, and planar plating morphology, which likely results from the intermediate formation of InSn<sub>4</sub> alloy phase (Figure S23, Supporting Information). It remains unclear whether the alloy formation is a universal law for planar plating or not, but the exploration and optimization of suitable substrates will be an interesting and promising direction for In metal batteries.

To elucidate the effect of substrates on the In plating, we conducted physical and electrochemical characterizations. As shown in Figure 4a, at a shallow plating depth (0.2-1 mAh cm<sup>-2</sup>), two characteristic peaks emerge at 34.5° and 60.1°, which are attributed to the InCu alloy phase. As plating progresses (5-10 mAh cm<sup>-2</sup>), the intensity of In metal increases, while the InCu alloy is present during the entire period. This suggests the in situ formation of InCu alloy preceding the In plating. Figure S24 (Supporting Information) shows the index of this InCu alloy, which adopts a monoclinic structure (JCPDS#00-035-1150). Cross-sectional SEM further corroborates the alloy formation. For better visualization, we selected the 10 mAh cm<sup>-2</sup> electrode for observation. As depicted in Figure 4b, the Cu element resides in the base of In@Cu composite, while the In element is distributed throughout the entire composite. This suggests that the Cu substrate contains appreciable amounts of InCu alloy, and the upper material is pure In metal. In contrast, no alloy formation is observed in the In@Ti electrode (Figure \$25, Supporting Information). We also monitored the interfacial composition and impedance change before and after cycling. Ex situ XRD analysis reveals that the InCu alloy is present throughout the cycling, suggesting battery interfacial stability (Figure S26, Supporting Information). Electrochemical impedance spectra (EIS) tests suggest that the charge-transfer resistance decreases from 0.13 to 0.10 ohm in the first 5 cycles and remains stable at 0.1 ohm afterward, which corroborates the interfacial stability (Figure \$27 and Table \$4, Supporting Information).

16163028, 0, Downloaded from https://onlinelibrary.wiley.com/doi/10.1002/adfm.202407342 by Jim Jim - University Of British Columbia , Wiley Online Library on [02.0072024]. See the Terms and Conditions (https://onlinelibrary.wiley.com/

md-conditions) on Wiley Online Library for rules of use; OA articles are governed by the applicable Creative Commons License

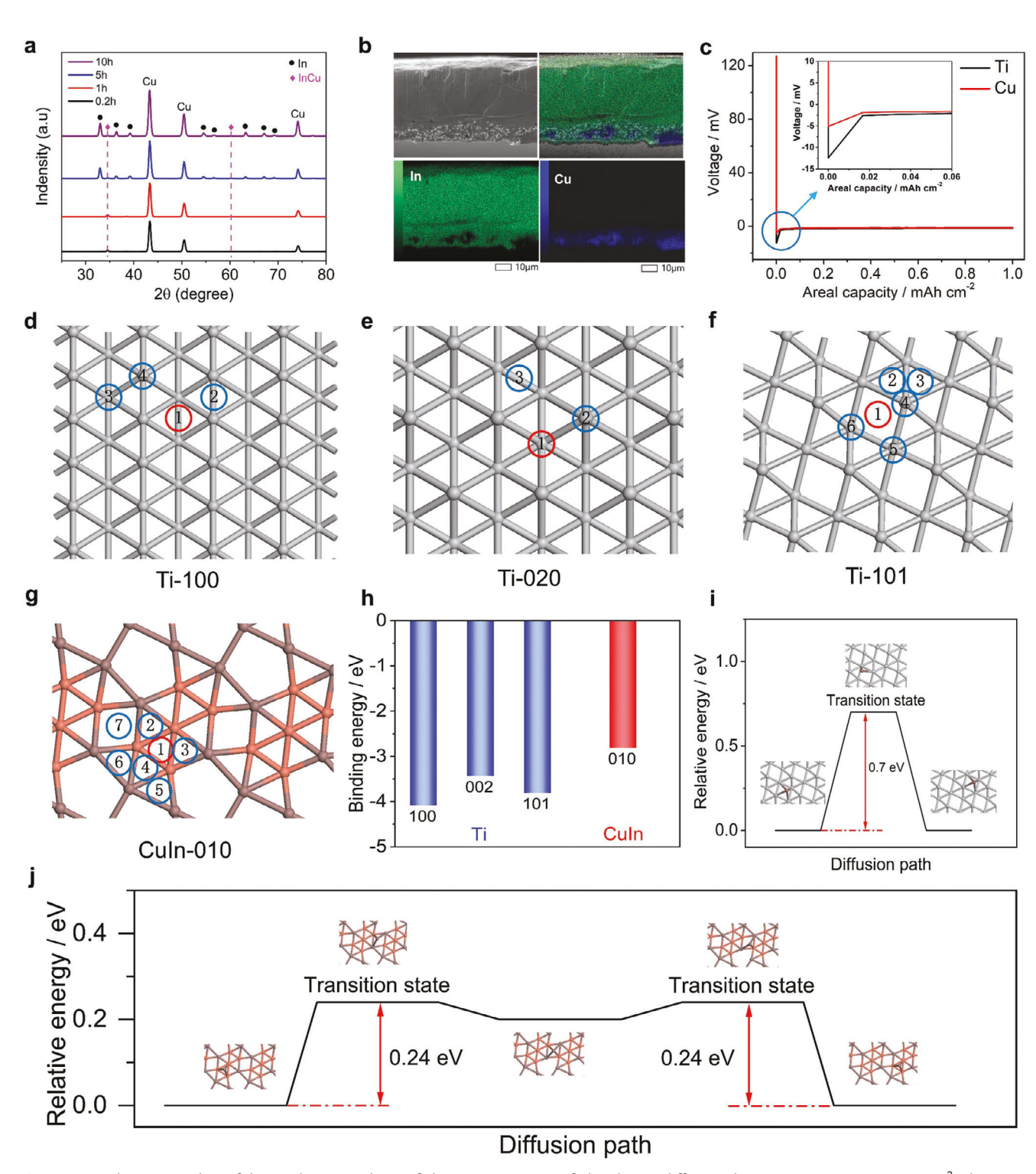


Figure 4. Mechanism studies of the In plating on the Cu foil: a) XRD patterns of plated In at different plating time (current: 1 mA cm<sup>-2</sup>). b) Cross-sectional SEM and mapping analysis of the plated In at 10 mAh cm<sup>-2</sup>. c) The polarization comparison between In||Ti and In||Cu batteries. d–g) The calculation models of indium absorbed on Ti and Cu substrate facets. h) The binding energy of indium absorption on Ti and Cu substrates. i,j) The indium diffusion pathway and energy barriers on the Ti (100) facet and the InCu (010) facet.

www.afm-journal.de

16163028, 0, Downloaded from https://onlineitbrary.wiley.com/doi/10.1002/adfm.202407342 by jim jim - University Of British Columbia , Wiley Online Library on [02.07/2024]. See the Terms and Conditions (https://onlineitbrary.wiley.com/erms

and-conditions) on Wiley Online Library for rules of use; OA articles are governed by the applicable Creative Commons Licens

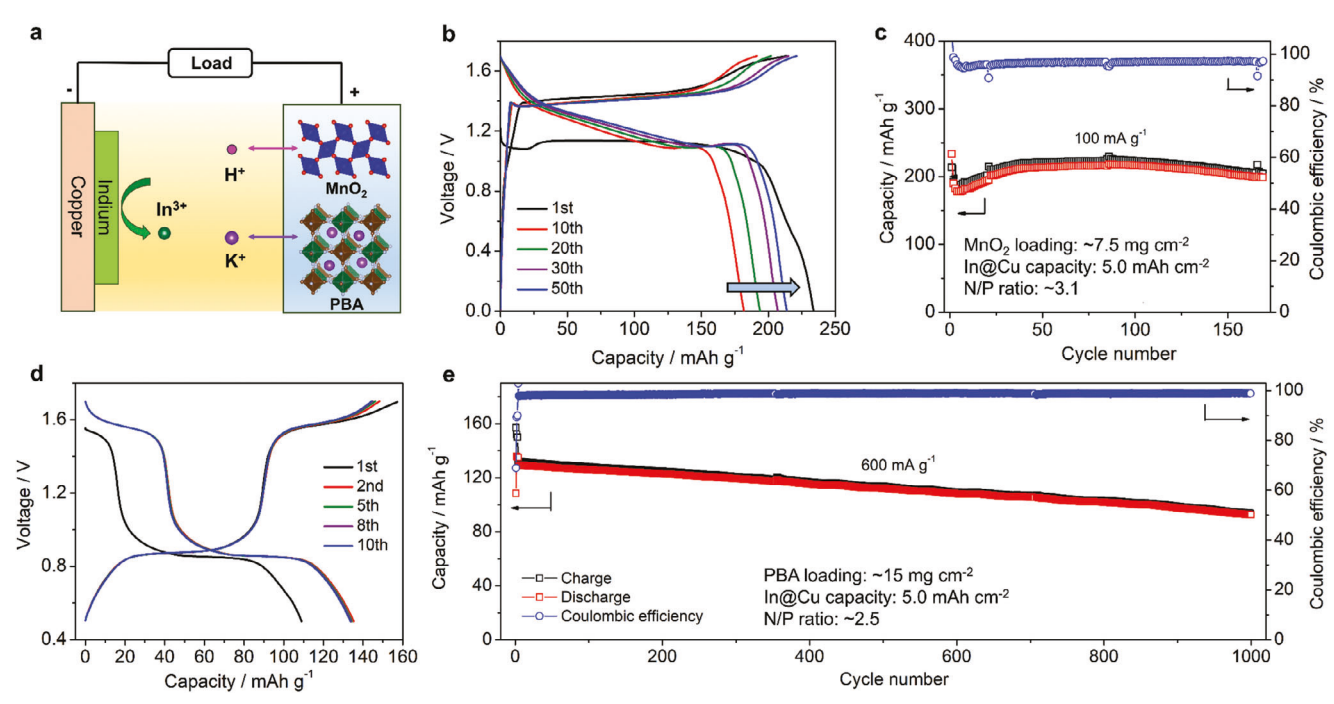


Figure 5. Aqueous In metal full cells. a) The battery working mechanism of  $In||MnO_2|$  and  $In||FeFe(CN)_6|$  batteries. b) GCD curves of  $In||MnO_2|$  at 100 mA  $g^{-1}$ . c) The cycling performance at 100 mA  $g^{-1}$ . d) GCD curves of  $In||FeFe(CN)_6|$  at 120 mA  $g^{-1}$ . e) The cycling performance at 600 mA  $g^{-1}$ .

The InCu alloy plays a critical role in achieving planar morphology. Firstly, it decreases the nucleation overpotential from  $\approx 15$  mV on Ti to  $\approx 5$  mV on Cu (Figure 4c). Recent studies<sup>[47,48]</sup> suggest that a lower overpotential is beneficial to create abundant and homogenous nucleation sites, which can facilitate the subsequent metal growth. Second, this InCu interface shows a favorable yet moderate binding energy toward In atoms, which results in a low energy barrier for the subsequent In atom diffusion along the planar direction.

To gain mechanistic insights into the In plating, we conducted DFT calculations to reveal the interactions between In atoms and substrates, examining both thermodynamics and kinetics. In our simulations, the (100), (002), and (101) planes of the Ti foil were selected due to their low surface energies. For the InCu alloy, we chose the experimentally observed (010) plane, supported by its highest diffraction intensity at  $\approx 34.5^{\circ}$  (Figure S24, Supporting Information).

Initially, we investigated the In atom adsorption on all possible adsorption sites. Figure 4d–g presents the thermodynamically most favorable sites marked with red circles. The In atom prefers the adsorption on the center of a triangle space in the InCu (010) plane with a rather low binding energy of -2.81 eV (Figure 4g). In comparison, all three binding sites on the Ti foil, namely, the edge of Ti (100) plane, the top of Ti (020) plane, and the center of the diamond space of Ti (101) plane, have even lower binding energies of -4.09, -3.43, and -3.80 eV, respectively (Figure 4h). These results suggest that from the thermodynamic perspective, the Ti foil should be more favorable for the initial In atom adsorption.

Subsequently, we investigated the In diffusion on both Ti foil and InCu alloy using the climbing image-nudged elastic band (CI-NEB) method.<sup>[61]</sup> The migration pathways of In atoms be-

tween adjacent stable sites were considered to examine the transport kinetics on the Ti (101) facet, which has the lowest In binding energy of -4.09 eV (Figure 4h), and the CuIn-010 facet. As illustrated in Figure 4i, the diffusion energy barrier for In migration is 0.70 eV on the Ti foil, whereas it is merely 0.24 eV on the InCu interface. Although the Ti foil thermodynamically favors the initial adsorption of In atoms, the high energy barrier hinders the subsequent In atom migration, thereby impeding the planar propagation of In atoms. In contrast, despite the InCu alloy having a moderate In binding energy, its much lower diffusion barrier facilitates the In layer growth.

The theoretical analyses shed light on the experimental observations of different morphologies. Although In atoms are more preferred to adsorb on the Ti surface with lower binding energies, the high diffusion energy barrier hinders the In migration to neighboring sites, which exerts a tendency to form "clusters". This can explain the observed particle-stacking morphology on the Ti foil. On the contrary, the InCu alloy demonstrates a moderate binding energy toward In atoms, while its reduced barrier for In atom diffusion fosters indiophilic properties. Consequently, plated In atoms readily migrate to the adjacent and neighboring sites along the InCu plane surface, resulting in planar foil-like morphology.

To harness the high efficiency and stability of In metal, we proposed two approaches for implementing full cells (**Figure 5a**). Firstly, a low-cost and earth-abundant manganese dioxide (MnO<sub>2</sub>) cathode can be used (Figure S28, Supporting Information), operating on H<sup>+</sup> ion insertion in this moderately acidic InCl<sub>3</sub> electrolyte. [62,63] Recently, the working mechanism of the In||MnO<sub>2</sub> battery has been elucidated, [64] which delivered a high capacity of  $\approx \! 330$  mAh g<sup>-1</sup> and stable cycling of 680 cycles. Nevertheless, the cathode mass loading is merely 1.5–2.0 mg cm<sup>-2</sup>,

ADVANCED FUNCTIONAL MATERIALS 1616928, D. Downloaded from https://onlinelibrary.wiley.com/doi/10.1002/adfm.202407342 by jim jim - University Of British Celumbia, Wiley Online Library on [02.07/2024]. See the Terms and Conditions (https://onlinelibrary.wiley.com/erms-and-conditions) on Wiley Online Library for rules of use; OA articles are governed by the applicable Creative Commons Licenses

and the In anode capacity is excessive (200  $\mu$ m,  $\approx$ 103 mAh cm<sup>-2</sup>), thus pertaining to a half cell. Therefore, we increased the MnO<sub>2</sub> loading to 7.5 mg cm<sup>-2</sup> and predeposited In on Cu foil with  $\approx$ 5.0 mAh cm<sup>-2</sup>. This full cell (N/P = 3.1) exhibits similar GCD curves to the previous report, [64] but it undergoes a capacity activation process (Figure 5b), possibly due to the precipitation and coverage of indium salts, such as InOCl and In2O3, as reported previously. [64] The capacity stabilizes at  $\approx$ 220 mAh g<sup>-1</sup>, with an average voltage of 1.2 V. After ≈170 cycles, the capacity fades to 204 mAh  $g^{-1}$  (Figure 5c), leading to a promising retention of 93%. To demonstrate the potential application of this In||MnO<sub>2</sub> battery, we assembled a pouch cell with a practically high mass loading of ≈50 mg cm<sup>-2</sup>. As shown in Figure \$29 (Supporting Information), this pouch cell exhibits an open circuit voltage of  $\approx 1.2 \text{ V}$ , which agrees well with the Swagelok cell data (Figure 5b). When two batteries are connected in series, they can successfully light a LED bulb (2-3 V range). Considering the energy and safety merits, aqueous In metal batteries may find potential applications in electric tools, electronics, and wearable devices.

Alternatively, it is feasible to fabricate hybrid In metal batteries, where additional salts and cations can be introduced. For demonstration purposes, we made a hybrid electrolyte of 1.0 м InCl<sub>3</sub> + 1.0 м potassium chloride (KCl), coupled with a Prussian blue cathode of FeFe(CN)<sub>6</sub> (Figure S30, Supporting Information), which is known to host K+ with fast kinetics and stable cycling.  $^{[65,66]}$  The active mass loading was further increased to  $\approx 15 \text{ mg cm}^{-2}$  (area capacity:  $\approx 2.0 \text{ mAh cm}^{-2}$ ), while the In@Cu electrode remained at  $5.0 \text{ mAh cm}^{-2}$ , leading to a N/P ratio of 2.5. Notably, the addition of 1.0 M K+ did not influence the In plating efficiency (Figure \$31, Supporting Information). As shown in Figure 5d, this hybrid battery demonstrates the characteristic GCD curve of FeFe(CN)<sub>6</sub>, with a discharge capacity of  $\approx$ 135 mAh  $g^{-1}$  and two voltage plateaus at  $\approx 1.6$  and  $\approx 0.85$  V. The identical cyclic voltammetry (CV) curves observed in both pure KCl and hybrid K<sup>+</sup>/In<sup>3+</sup> electrolytes further confirm the K<sup>+</sup> insertion on the cathode (Figure S32, Supporting Information).

This hybrid  $In||FeFe(CN)_6$  battery shows a high rate capability and long cycling life. At a high current density of 3600 mA  $g^{-1}$ , the battery retains a good capacity of 92 mAh  $g^{-1}$  and a capacity utilization of 70%, which likely stems from the large open Prussian blue structure with fast  $K^+$  insertion kinetics (Figure S33, Supporting Information). When this battery is cycled at a moderate current of 360 mA  $g^{-1}$ , the discharge capacity fades from 130 to 105 mAh  $g^{-1}$  after 450 cycles, corresponding to a high retention of 81.0% (Figure S34, Supporting Information). At a higher current density of 600 mA  $g^{-1}$ , the full cell achieves an extended cycling life of 1000 cycles (Figure 5e), with a capacity retention of 72%. These results underscore the effectiveness of In metal in building high-performance aqueous trivalent metal full cells.

#### 3. Conclusion

In summary, we studied the effect of substrates on the plating behavior of trivalent indium metal, and we achieved a uniform, planar, and flat morphology with a simple Cu foil substrate. This morphology results from the formation of an indiophilic InCu alloy interface, which reduces the nucleation barriers and facilitates the nucleation process. Consequently, the planar In metal delivers an ultrahigh efficiency of 99.80–99.90% across various

conditions (1–10 mAh cm $^{-2}$ ; 1–4 mA cm $^{-2}$ ) and demonstrates an excellent calendar life of 6.4–7.4 months, surpassing the performance of Al and Sb candidates. The high efficiency and long lifespan is further validated through the implementation of In||MnO<sub>2</sub> and In||FeFe(CN)<sub>6</sub> full cells, where excellent cycling is achieved with thick electrodes and limited N/P ratios. Our work reveals the efficacy of exploiting indium as an advanced metal for aqueous trivalent batteries.

## 4. Experimental Section

Material Synthesis: The FeFe(CN) $_6$  cathode material was prepared using a solution-based precipitation method. Specifically, 40 mL of 0.1 m  $K_3$ Fe(CN) $_6$  solution was slowly added to 80 mL of 0.1 m FeCl $_3$  solution under magnetic stirring, and the solution was maintained at 60 °C for 6 h. After cooling to room temperature, the precipitate was obtained by centrifugation, washed several times with deionized water and ethanol, and finally dried in an oven at 60 °C. The MnO $_2$  cathode material was commercially available (HiMedia, >99.0% purity).

Indium particles were synthesized by a chemical reduction method. In a typical synthesis, 0.1 g of polyvinyl pyrrolidone (PVP, K-30) was dissolved in 3 mL of ethanol. Subsequently, 0.05 g of InCl $_3$  was added to the solution, which was then purged with nitrogen gas to create an inert atmosphere. The mixture was stirred for 10 min to ensure complete dissolution of the InCl $_3$  in the two-neck flask. A separate solution of sodium borohydride (0.03 g NaBH $_4$  in 10 mL H $_2$ O) was added dropwise to the InCl $_3$  solution using a glass syringe under constant stirring. The resulting mixture solution was stirred for 3 h, and the obtained indium particles were centrifuged and washed five times with ethanol and water. The final particles were allowed to dry at 60 °C in a vacuum oven.

Physical Characterization: X-ray diffractometry (XRD) profiles of the FeFe(CN)<sub>6</sub> powders and self-standing film electrodes, the MnO<sub>2</sub> material, and In–Cu alloy composition were acquired using the Rigaku Supernova instrument. This instrument was equipped with a HyPix3000 X-ray sensor and Cu-Kα radiation source ( $\lambda$  = 1.5406 Å). Imaging and elemental mapping of the FeFe(CN)<sub>6</sub> materials and electrodes, as well as indium metals, were conducted using scanning electron microscopy (SEM) with energy dispersive X-ray spectroscopy (EDX) at a field emission scanning electron microscope (SEM, JEOL, JSM-6480LV).

Electrode Preparation: For the FeFe(CN)<sub>6</sub> electrode, FeFe(CN)<sub>6</sub> powders were initially ground with Ketjen carbon in a 7:2 mass ratio. Subsequently, the composites were mixed with polytetrafluoroethylene (PTFE) binder in a 7:2:1 mass ratio and rolled into a self-standing film. The active mass loading for FeFe(CN)<sub>6</sub> is  $\approx 15~\text{mg cm}^{-2}$ . For the MnO<sub>2</sub> electrode, MnO<sub>2</sub> powders were ground with Ketjen black in an 8:1 mass ratio. Polyvinylidene fluoride (PVDF) binder solution was then added to form a slurry in an 8:1:1 ratio. The slurry was cast onto the carbon fiber paper and dried in an oven at 60 °C. The active mass loading for MnO<sub>2</sub> is  $\approx 7.5~\text{mg}\,\text{cm}^{-2}$ 

Battery Assembly and Testing: The indium foil (99.99% purity, 0.2 mm thickness) was cut into circular-shaped pieces (Ø = 5/8 in., approximately 1.98 cm $^{-2}$  area) for utilization. Asymmetric In||Ti cells and In||Cu cells were fabricated in the 2032 coin cells, employing a high-purity Ti foil (0.03 mm thick) and Cu foil (9  $\mu m$  thick) as the working electrode, respectively. The In metal was used as the counter and reference electrode. The Sn foil (98.8% purity, 0.25 mm thickness) was purchased from Sigma Aldrich. The In||Sn battery was assembled in a similar way to the In||Cu battery The electrolyte consisted of a 1.0  $\mu$  aqueous solution of InCl $_3$  (Sigma Aldrich), with a volume of 100  $\mu$ L.

The In–FeFe(CN) $_6$  batteries were assembled in Swagelok cells with a mixture solution of 1 m KCl + 1 m InCl $_3$ , utilizing titanium rods as the current collectors. Similarly, the In–MnO $_2$  batteries were also assembled in Swagelok cells, using the 1.0 m InCl $_3$  electrolyte. 5.0 mAh cm $^{-2}$  In metal was deposited on the Cu foil and used it as the counter electrode for In–FeFe(CN) $_6$  and In–MnO $_2$  full cells. To assemble the pouch cell, we made a self-standing MnO $_2$  electrode with a practically high mass loading of

1616208.9, D. Downloaded from https://onlinelibrary.wiley.com/doi/10.1002/adfm.202407342 by jim jim - University Of British Columbia, Wiley Online Library on [02.07/2024]. See the Terms and Conditions (https://onlinelibrary.wiley.com/errers-ad-conditions) on Wiley Online Library for rules of use; OA articles are governed by the applicable Certain Commons

 $\approx$ 50 mg cm<sup>-2</sup>, and it was pressed on the Ti mesh current collector. The anode is a large piece of In metal foil (200 µm thickness). Two layers of glass fibers were used as the separator. The cathode and anode were sandwiched by separators, added with InCl<sub>3</sub> electrolytes, transferred into the aluminum-laminated bag, and then sealed with a heat sealer.

Galvanostatic charge/discharge tests were conducted using the Landt battery tester (CT3002AU) at room temperature. Cyclic voltammetry, linear sweep voltammetry curves, and electrochemical impedance results were obtained using a Biologic SP-150 Potentiostat.

DFT Calculations: The spin-polarized density function theory (DFT) was performed using the Vienna ab initio simulation package (VASP).[67] The projector augmented wave (PAW) method was used to describe coresvalance electrons interaction, and the Perdew-Burke-Ernzerhof (PBE) functional based on the generalized gradient approximation (GGA) was implemented to describe the exchange-correlation energy  $[^{6\hat{8},69]}$  The Brillouin zone was sampled by the Gamma scheme and the k points setting was changed based on different facets to achieve the precision requirement (at least 0.015 1  $\mbox{\AA}^{-1}$  in actual space). The energy cutoff was set to 550 eV, and the convergence tolerance of energy and force were set as  $10^{-5}$  eV per atom and 0.01 eV per angstrom, respectively. The van der Waals interactions were considered using the DFT-D3 method with the Becke-Johnson damping function, [70,71] and a vacuum space of more than 15 Å was applied to avoid the interaction from periodic conditions.

To investigate the Indium growth process, the binding energy  $(E_b)$  was calculated via the formula:

$$E_{b} = E_{sub+ln} - E_{sub} - E_{ln} \tag{1}$$

where  $E_{\text{sub+In}}$  and  $E_{\text{sub}}$  are the total energies of exposed metal surface with/without Indium adsorption, while the  $E_{\rm ln}$  presents the energy of a free Indium atom. The climbing image-nudged elastic band (CI-NEB) method was also performed to obtain the free energy barrier between the most stable indium adsorption sites.[61]

#### **Supporting Information**

Supporting Information is available from the Wiley Online Library or from the author.

## Acknowledgements

The authors thank the financial support from the NSF Center for the Advancement of Wearable Technologies (grant no. 1849243) and NASA MIRO PR-SPRINT (grant no. 80NSSC19M0236).

# **Conflict of Interest**

The authors declare no conflict of interest.

# **Data Availability Statement**

The data that support the findings of this study are available in the Supporting Information of this article.

#### Keywords

aqueous trivalent metal batteries, indium-copper alloy, indium metal anode, planar plating, ultrahigh efficiency

> Received: April 29, 2024 Revised: June 18, 2024 Published online:

- [1] J. Liu, Z. Bao, Y. Cui, E. J. Dufek, J. B. Goodenough, P. Khalifah, Q. Li, B. Y. Liaw, P. Liu, A. Manthiram, Nat. Energy. 2019, 4, 180.
- [2] M. Armand, J. M. Tarascon, Nature. 2008, 451, 652.
- [3] X. Ji, Energy Environ. Sci. 2019, 12, 3203.
- [4] J. B. Goodenough, K.-S. Park, J. Am. Chem. Soc. 2013, 135, 1167.
- [5] J. W. Choi, D. Aurbach, Nat. Rev. Mater. 2016, 1, 16013.
- [6] Z. Pan, X. Liu, J. Yang, X. Li, Z. Liu, X. J. Loh, J. Wang, Adv. Energy Mater. 2021, 11, 2100608.
- [7] Y. Liu, G. He, H. Jiang, I. P. Parkin, P. R. Shearing, D. J. L. Brett, Adv. Funct. Mater. 2021, 31, 2010445.
- [8] C. Wei, J. Song, Y. Wang, X. Tang, X. Liu, Adv. Funct. Mater. 2023, 33, 2304223.
- [9] Y. Wang, J. Yi, Y. Xia, Adv. Energy Mater. 2012, 2, 830.
- [10] D. Bin, F. Wang, A. G. Tamirat, L. Suo, Y. Wang, C. Wang, Y. Xia, Adv. Energy Mater. 2018, 8, 1703008.
- [11] J. Zhu, Z. Bie, X. Cai, Z. Jiao, Z. Wang, J. Tao, W. Song, H. J. Fan, Adv. Mater. 2022. 34, 2207209.
- [12] L. Zhang, B. Zhang, T. Zhang, T. Li, T. Shi, W. Li, T. Shen, X. Huang, J. Xu, X. Zhang, Z. Wang, Y. Hou, Adv. Funct. Mater. 2021, 31, 2100186.
- [13] X. Zhang, L. Zhang, X. Jia, W. Song, Y. Liu, Nano-Micro Lett. 2024, 16,
- [14] L. Ma, Q. Li, Y. Ying, F. Ma, S. Chen, Y. Li, H. Huang, C. Zhi, Adv. Mater. 2021, 33, 2007406.
- [15] X. Wu, A. Markir, Y. Xu, C. Zhang, D. P. Leonard, W. Shin, X. Ji, Adv. Funct. Mater. 2019, 29, 1900911.
- [16] Z. He, F. Xiong, S. Tan, X. Yao, C. Zhang, Q. An, Mater. Today Adv.
- 2021, 11, 100156. [17] J. Liu, D. Dong, A. L. Caro, N. S. Andreas, Z. Li, Y. Qin, D. Bedrov, T.
- Gao, ACS Cent. Sci. 2022, 8, 729. [18] C. Bai, H. Jin, Z. Gong, X. Liu, Z. Yuan, Energy Storage Mater. 2020,
- 28, 247. [19] J. Zhao, X. Yang, S. Li, N. Chen, C. Wang, Y. Zeng, F. Du, CCS Chem.
- 2021, 3, 2498.
- [20] S. Bi, S. Wang, F. Yue, Z. Tie, Z. Niu, Nat. Commun. 2021, 12, 6991.
- [21] M. Wang, Y. Meng, P. Gao, K. Li, Z. Liu, Z. Zhu, M. Ali, T. Ahmad, N. Chen, Y. Yuan, Adv. Mater. 2023, 35, 2305368.
- [22] Q. Yang, X. Qu, H. Cui, X. He, Y. Shao, Y. Zhang, X. Guo, A. Chen, Z. Chen, R. Zhang, Angew. Chem., Int. Ed. 2022, 61, e202206471.
- [23] S. Bi, Y. Zhang, S. Deng, Z. Tie, Z. Niu, Angew. Chem., Int. Ed. 2022, 61, e202200809.
- [24] M. Wang, Y. Meng, Y. Xu, N. Chen, M. Chuai, Y. Yuan, J. Sun, Z. Liu, X. Zheng, Z. Zhang, Energy Environ. Sci. 2023, 16, 5284.
- [25] X. Wu, A. Markir, L. Ma, Y. Xu, H. Jiang, D. P. Leonard, W. Shin, T. Wu, J. Lu, X. Ji, Angew. Chem., Int. Ed. 2019, 58, 12640.
- [26] C. Dai, L. Hu, H. Chen, X. Jin, Y. Han, Y. Wang, X. Li, X. Zhang, L. Song, M. Xu, Nat. Commun. 2022, 13, 1863.
- [27] J. Zhang, X. Zhang, C. Xu, H. Yan, Y. Liu, J. Xu, H. Yu, L. Zhang, J. Shu, Adv. Energy Mater. 2022, 12, 2103998.
- [28] G. Liang, F. Mo, Q. Yang, Z. Huang, X. Li, D. Wang, Z. Liu, H. Li, Q. Zhang, C. Zhi, Adv. Mater. 2019, 31, 1905873.
- [29] H. Cai, S. Bi, R. Wang, L. Liu, Z. Niu, Angew. Chem., Int. Ed. 2022, 61, e202205472.
- [30] Y. Liang, H. Dong, D. Aurbach, Y. Yao, Nat. Energy. 2020, 5, 646.
- [31] C. Pieremanuele, S. G. Gopalakrishnan, M. Rahul, L. Miao, C. Gerbrand, Chem. Rev. 2017, 117, 4287.
- [32] X. Zheng, C. Han, C.-s. Lee, W. Yao, C. Zhi, Y. Tang, Prog. Mater. Sci. 2024, 143, 101253.
- [33] R. Stephanie, C. Y. Park, P. A. Shinde, E. Alhajri, N. R. Chodankar, T. J. Park, Energy Storage Mater. 2024, 68, 103336.
- [34] N. M. Laptash, E. V. Kovaleva, A. A. Mashkovskii, A. Y. Beloliptsev, L. A. Zemnukhova, J. Struct. Chem. 2007, 48, 848.
- [35] D. W. Barnum, Inorg. Chem. 1983, 22, 2297.



www.advancedsciencenews.com



www.afm-journal.de

16163028, 0, Downloaded from https://onlinelibrary.wiley.com/doi/10.1002/adfm.202407342 by jim jim - University Of British Columbia, Wiley Online Library on [02.07/2024]. See the Terms and Conditions

on Wiley Online Library for rules of use; OA articles are governed by the applicable Creative Co.

- [36] B. W. Zhang, L. Ren, Y. X. Wang, X. Xu, Y. Du, S. X. Dou, Interdiscip. Mater. 2022, 1, 354.
- [37] Z. Wang, J. Huang, Z. Guo, X. Dong, Y. Liu, Y. Wang, Y. Xia, Joule. 2019, 3, 1289.
- [38] J. Zheng, D. C. Bock, T. Tang, Q. Zhao, J. Yin, K. R. Tallman, G. Wheeler, X. Liu, Y. Deng, S. Jin, Nat. Energy. 2021, 6, 398.
- [39] Y. An, Y. Tian, K. Zhang, Y. Liu, C. Liu, S. Xiong, J. Feng, Y. Qian, Adv. Funct. Mater. 2021, 31, 2101886.
- [40] D. Tabor, The Hardness of Metals, Oxford University Press, Oxford 2000.
- [41] S. D. Pu, C. Gong, Y. T. Tang, Z. Ning, J. Liu, S. Zhang, Y. Yuan, D. Melvin, S. Yang, L. Pi, Adv. Mater. 2022, 34, 2202552.
- [42] S. Chen, Y. Xia, R. Zeng, Z. Luo, X. Wu, X. Hu, J. Lu, E. Gazit, H. Pan, Z. Hong, Sci. Adv. 2024, 10, eadn2265.
- [43] S. Trasatti, J. Electroanal. Chem. Interfacial Electrochem. 1972, 39, 163.
- [44] A. B. Laursen, A. S. Varela, F. Dionigi, H. Fanchiu, C. Miller, O. L. Trinhammer, J. Rossmeisl, S. Dahl, J. Chem. Educ. 2012, 89, 1595.
- [45] P. Quaino, F. Juarez, E. Santos, W. Schmickler, Beilstein J. Nanotechnol. 2014, 5, 846.
- [46] B. Li, K. Yang, J. Ma, P. Shi, L. Chen, C. Chen, X. Hong, X. Cheng, M. C. Tang, Y. B. He, Angew. Chem., Int. Ed. 2022, 61, e202212587.
- [47] Q. Zhang, J. Luan, L. Fu, S. Wu, Y. Tang, X. Ji, H. Wang, Angew. Chem., Int. Ed. 2019, 58, 15841.
- [48] K. Yan, Z. Lu, H.-W. Lee, F. Xiong, P.-C. Hsu, Y. Li, J. Zhao, S. Chu, Y. Cui, Nat. Energy. 2016, 1, 16010.
- [49] S. R. Kumar, B. Prajapati, S. K. Tiwari, V. K. Tiwari, *Indian J. Pure Appl. Phys.* 2008, 46, 198.
- [50] P. R. Subramanian, D. E. Laughlin, Bull. Alloy Phase Diagrams. 1989, 10, 554.
- [51] X. Ji, L. F. Nazar, Nat. Sustainability. 2024, 7, 98.
- [52] L. Ma, M. A. Schroeder, O. Borodin, T. P. Pollard, M. S. Ding, C. Wang, K. Xu, Nat. Energy. 2020, 5, 743.

- [53] C. Yan, C. Lv, B.-E. Jia, L. Zhong, X. Cao, X. Guo, H. Liu, W. Xu, D. Liu, L. Yang, J. Am. Chem. Soc. 2022, 144, 11444.
- [54] Q. Hao, F. Chen, X. Chen, Q. Meng, Y. Qi, N. Li, ACS Appl. Mater. Interfaces. 2023, 15, 34303.
- [55] Q. Ran, H. Shi, H. Meng, S.-P. Zeng, W.-B. Wan, W. Zhang, Z. Wen, X.-Y. Lang, Q. Jiang, Nat. Commun. 2022, 13, 576.
- [56] C. Yan, C. Lv, L. Wang, W. Cui, L. Zhang, K. N. Dinh, H. Tan, C. Wu, T. Wu, Y. Ren, J. Am. Chem. Soc. 2020, 142, 15295.
- [57] A. Ejigu, L. W. Le Fevre, A. Elgendy, B. F. Spencer, C. Bawn, R. A. W. Dryfe, ACS Appl. Mater. Interfaces. 2022, 14, 25232.
- [58] Y. Yu, R. Qin, X. Shi, J. Xie, T. H. Lu, X. Lu, Battery Energy. 2023, 2, 20230016.
- [59] F. Wang, J. Xie, D. Zheng, F. Yang, H. Zhang, X. Lu, Adv. Mater. 2022, 34, 2200085.
- [60] Y. Yu, J. Xie, L. Zhou, F. Yang, H. Zhang, X. Liu, P. Yu, X. Lu, Energy Storage Mater. 2022, 49, 529.
- [61] G. Henkelman, B. P. Uberuaga, H. Jónsson, J. Chem. Phys. 2000, 113, 9901.
- [62] H. Pan, Y. Shao, P. Yan, Y. Cheng, K. S. Han, Z. Nie, C. Wang, J. Yang, X. Li, P. Bhattacharya, Nat. Energy. 2016, 1, 16039.
- [63] W. Liu, X. Zhang, Y. Huang, B. Jiang, Z. Chang, C. Xu, F. Kang, J. Energy Chem. 2021, 56, 365.
- [64] S. Chang, J. F. F. Gomez, S. Katiyar, G. Morell, X. Wu, J. Am. Chem. Soc. 2023, 145, 24746.
- [65] W. Ren, X. Chen, C. Zhao, Adv. Energy Mater. 2018, 8, 1801413.
- [66] X. Wu, Y. Xu, H. Jiang, Z. Wei, J. J. Hong, A. S. Hernandez, F. Du, X. Ji, ACS Appl. Energy Mater. 2018, 1, 3077.
- [67] G. Kresse, J. Furthmüller, Phys. Rev. B. 1996, 54, 11169.
- [68] J. P. Perdew, K. Burke, M. Ernzerhof, Phys. Rev. Lett. 1996, 77, 3865.
- [69] P. E. Blöchl, Phys. Rev. B: Condens. Matter Mater. Phys. 1994, 50, 17953.
- [70] S. Grimme, J. Antony, S. Ehrlich, H. Krieg, J. Chem. Phys. 2010, 132.
- [71] S. Grimme, S. Ehrlich, L. Goerigk, J. Comput. Chem. 2011, 32, 1456.